Thermal Emission with High Temporal and Spatial Coherence by Harnessing Quasiguided Modes

Kaili Sun,[1] Uriel Levy,[2] and Zhanghua Han[1,*]

[1] *Shandong Provincial Key Laboratory of Optics and Photonic Devices, Center of Light Manipulation and Applications, School of Physics and Electronics, Shandong Normal University, Jinan 250358, China*
[2] *Department of Applied Physics, The Hebrew University of Jerusalem, Jerusalem 91904, Israel*

(Received 27 March 2023; revised 22 May 2023; accepted 21 July 2023; published 14 August 2023)

Thermal emissions with both narrow spectral bandwidth and compressed angular distributions suggesting high temporal and spatial coherence are useful for the realization of an alternative family of highly efficient optical devices, and they play an increasingly significant role in numerous applications. Although people have endeavored to realize thermal emitters by harnessing different physics implemented in various artificial metasurfaces mainly made from metals, most of the reported results to date fail to produce emitters possessing the above merits. This work presents a proof-of-principal experimental demonstration on how to make use of the concept of quasiguided modes to realize alternative thermal mid-infrared emitters. Supported by an elaborately designed binary grating structure containing a period-doubling perturbation, these modes possess ultrahigh and perturbation-dependent Q factors. Although an amorphous form of evaporated materials is used, and the measured signal is a superposition of multiangle emission peaks, an emission bandwidth of about 25 nm is still experimentally obtained at the wavelength of 5.8 μm, which is one order of magnitude smaller than conventional thermal emitters based on metallic metamaterials. This bandwidth implies that a similar level of enhancement in the temporal coherence is achieved. Furthermore, our calculations show that the thermal emissions based on the quasiguided modes can achieve a spatial coherence length of 1.7 mm. Both of these two coherence properties are the state of the art to date in the mid-infrared thermal emitters.

DOI: 10.1103/PhysRevApplied.20.024033

I. INTRODUCTION

Mid-infrared (MIR) thermal emissions result from various thermal fluctuations in the object, and are thus broadband, omnidirectional, and usually considered as noncoherent. How to use artificial approaches to selectively enhance particular processes in regular thermal emissions to eventually achieve output radiations featuring controlled characteristics in, e.g., the spectral bandwidth, beam profile, spatial distribution, polarization, etc., represent an alternative research paradigm [1,2]. Thermal emissions with specially controlled characteristics may find special applications in various circumstances. For example, MIR radiation sources play a vital role in many sensing areas, e.g., industrial control [3], gas sensing [4], medical diagnosis [5], etc. Many substances especially those with small molecules exhibit unique absorption spectral features in this band, so the MIR is widely recognized as a molecular fingerprint region. In practical applications, although quantum cascade lasers (QCLs) [6] with pure spectral information and the advantage of single-mode operation are widely used as high-power MIR sources, their complex manufacturing process and high cost limit their application in many fields, which forces people to look for more economical alternatives. Conventional nondispersive infrared (NDIR) systems typically use broadband blackbody thermal emitters (e.g., miniatured light bulbs or globar) as the light source, while many target substances have narrow absorption linewidths. So ultranarrow band filters must be designed and employed in order to fully resolve the complex absorption spectral information, and a large amount of out-of-band emission is wasted. In addition, for a thermal radiation source with a fixed geometry, the tunability of the radiation wavelength in the broadband range is also relevant, which enables a flexible detection of a wide range of substances. Therefore, thermal emitters that have both characteristics of narrow bandwidth (i.e., high temporal coherence) and large spectral tunability are not only an essential component in the next-generation infrared sensing systems, but can also help reduce the cost and greatly improve the energy efficiency of current radiation sources.

Artificial micro- and nanostructures have been one of the most widely used platforms for realizing narrowband thermal radiation sources in recent years [7]. Usually, there

*zhan@sdnu.edu.cn

is a thick metal layer at the bottom of the structure used to work as the opaque substrate. According to Kirchhoff's law of thermal radiation, when the structure is heated to a high temperature and reaches a thermal equivalent state, it will generate thermal radiations with the same electromagnetic characteristics as the absorbed signals. At this time, the emission bandwidth of the entire structure is mainly determined by the electromagnetic characteristic of the structure, which, together with the temperature, also determines the absolute emissivity. A typical metamaterial structure to this end has the metal-insulator-metal (*M-I-M*) sandwich geometry [8]. In this configuration, the top layer of patterned metallic elements determine the resonance frequency while the thickness of the central spacer layer should be adjusted to provide an impedance matching between the structure and the environment to optimize the resonance emissivity and absorptivity. However, this kind of emitter usually suffers from broad emission peaks (experimentally, $Q < 40$) due to two effects: the strong dissipation of metals in the operation band at higher frequencies (e.g., in the IR or even visible) and the large radiation loss due to the poor modal confinement within the spacer layer between the two metal regions. There are also many other attempts to employ other physical mechanisms to realize ultranarrow band or wavelength-tunable MIR thermal radiation sources. For example, a groundbreaking research in 2002 demonstrated the introduction of grating structure into the SiC polar material to generate surface phonon polaritons (SPhPs) to achieve narrow bandwidth directional thermal emitters [9]. Unfortunately, the lattice vibrations inherent to polar crystals result in a limited operating spectral range of the emitter (10.5–12.5 μm). Quite recently, narrow bandwidth and spectrally tunable thermal emitters using the moiré effect in the twisted double-layer grating structure on the tungsten substrate were proposed [10], but the complex geometry of this structure makes it challenging to realize and control in the experiment. Some researchers have introduced phase-change materials to achieve narrowband thermal emission and the spectral tunability is achieved by changing the temperature to regulate their dielectric constants [11]. But these kinds of emitters can only work at specific temperatures with poor stability. Finally, the multilayer-film structures based on Tamm plasmon polariton [12,13] supports, in principal, narrow linewidth, but the influence due to the metal absorption is still strong and it is also difficult to tune the emission wavelength.

From the above analysis of the sandwich structure, we note that the bandwidth is affected by both the material absorption and radiation loss. While more attention is paid on the former, less work is done to manipulate the latter, which actually plays a more significant role at lower frequencies where the metals approach the perfect electric conductor more closely. In this paper, we introduce our recently proposed concept of quasiguided modes (QGMs) [14] with high Q factors into MIR thermal emitters for the first time to engineering the radiation loss to achieve ultranarrow bandwidth thermal emissions. It is known that to achieve thermal emissions with large coherence, the thermal fluctuations should couple to a nonlocal resonance of periodic optical elements so that they can travel over a large distance before coupling to the external [1]. The QGMs are a collective behavior in periodic structures where a period-doubling perturbation is introduced. This perturbation in one-dimensional (1D) gratings can be achieved by an increase of the width of every second element or a shift of its position. Under this perturbation, the sudden change in the lattice period leads to a halving of the first Brillouin zone (FBZ) and an associated band-folding effect. As a result, the guided modes (GMs) by the original structure with no coupling to free-space radiations will experience a flipping of the dispersion diagrams to be above the light cone to form alternative leaky states. Since the other modes inherit the same dispersion profiles of the GMs, they are referred to as QGMs. The Q factors of the QGMs can be engineered by the level of perturbation and the maintenance of ultrahigh Q factors can be made for all the resonances on the entire dispersion curve over a broad bandwidth and a large range of wave vectors. For lossless dielectric structures, when the period-doubling perturbation vanishes, the Q factor will approach infinity, in a similar way as the restoring of quasibound states in the continuum (QBIC) modes to ideal BIC [15,16]. However, the difference is that the BIC exists only at a very few discrete points in the ω–k space, whereas the QGMs will restore to GMs with infinite Q factors at any frequency point on the entire dispersion curve. The infinite Q factors of the GMs result from their dispersion diagrams below the light cone and cannot be excited by free-space radiations. Although a similar band-folding effect was proposed in earlier years and it was proposed to improve the angular tolerance in the reflection spectrum of resonant grating filters with doubly period structure [17,18], the use of this effect to generate alternative leaky modes with ultrahigh Q factors over a large bandwidth has been rarely investigated. Since the Q factor is intrinsically connected with the local electric field enhancement [19], the QGMs provide a good platform in manipulating the strong interaction of light and matter.

We will show that the broadband thermal fluctuations will couple to the nonlocal mode of QGMs to achieve the narrowband thermal emission. The QGMs are supported by a binary ridge grating on a slab waveguide placed on top of a metallic reflector. The binary grating is realized by changing the width of every second ridge, whose difference with the first ridge determines the Q factors of the QGMs and the final emission bandwidth. We first employed full-wave computational tools to design the structural parameters and analyzed the emission properties by using the absorption instead based on Kirchhoff's law.

After that, the manufacturing of the designed emitter is accomplished using standard nanofabrication techniques. The whole device is put into a special emission apparatus, which can be heated to different high temperatures, and then the characterization of the emission properties is performed and analyzed by using a Fourier-transformed infrared (FTIR) spectroscopy.

II. STRUCTURE AND RESULTS

The schematic structure of our proposed thermal emitter and an overview of the thermal emission process are summarized in Fig. 1. In our designed structure of the binary grating to support QGMs, Ge with both high refractive index and low loss in the MIR is used as the constituent material for the top grating layer as well as the waveguide core, and the bottom layer is an optically thick layer of gold [20]. A layer of refractory material of Al_2O_3 with low index [21] is used under the core layer to work as a spacer. In addition, the field distribution is mainly confined within the Ge slab, while the Al_2O_3 is used to minimize the influence of Au absorption to the waveguide mode. The top right inset shows the cross section of the unit cell of the binary grating. Through careful designing, a set of geometrical parameters are chosen as $P = 850$ nm, $t_1 = 610$ nm, $t_2 = 520$ nm, $h = 230$ nm, and $w = 270$ nm. The period P of the structure, and the size of the ridges including h and w will determine the radiation wavelength from the slab to the free space, while the ridge width difference δ determine the radiation Q factor of the whole structure. The Al_2O_3 thickness t_1 of the bottom layer can be adjusted to provide the impedance matching of the whole device with the environment to optimize the emissivity (see Supplemental Material [22] for all the material refractive-index parameters used in the calculation). According to Kirchhoff's law of thermal radiation, the emissivity for any object is equal to the absorptivity under thermodynamic equilibrium conditions. So in the calculation, the emissivity at a wavelength λ can be equivalently characterized by the absorptivity $E(\lambda) = A(\lambda) = 1 - R(\lambda) - T(\lambda)$, which can be further simplified as $E(\lambda) = A(\lambda) = 1 - R(\lambda)$, considering the presence of the opaque substrate. Therefore, in principle, one needs only to calculate the reflection characteristics of the thermal emitter structure shown in Fig. 1 to study the emission property. In the experiment, one can simply increase the temperature of the whole device or apply some electric current to the bottom metal layer to make it work as a Joule heater. The structure will emit thermal radiation with the same electromagnetic properties as the absorptivity. This method is widely used in the study of thermal radiation of various metamaterials.

In order to articulate the dependence of the Q factor of the supported QGMs on the value of δ, we start from a regular slab waveguide, which is schematically shown in Fig. 2(a). The slab waveguide supports the GMs whose dispersion diagram is located in the region below the light cone, which suggests that these modes cannot escape outward or be excited by free-space radiations. The Q factors for any frequency on the dispersion diagrams can be considered as infinite. When a periodic structure with the period P is introduced on the slab waveguide to modulate the refractive index [shown in Fig. 2(b)], the coupling between two counterpropagating modes leads to a spectral gap at the boundary of the FBZ at $k_x = \pi/P$ [23]. A similar spectral gap also appears in the

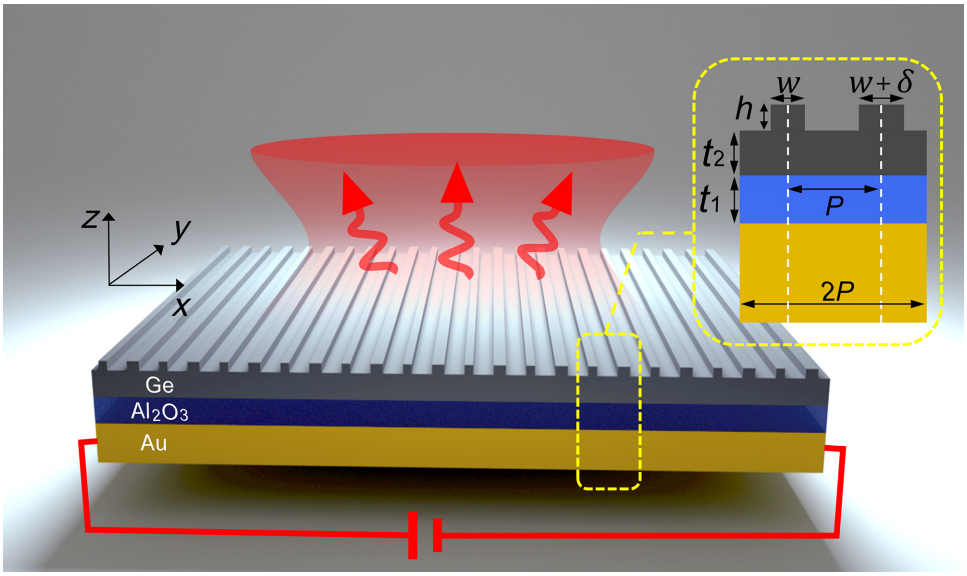

FIG. 1. Schematic diagram of the binary grating working as the thermal emitters based on the band-folding effect, with the red output beam indicating the thermal emissions.

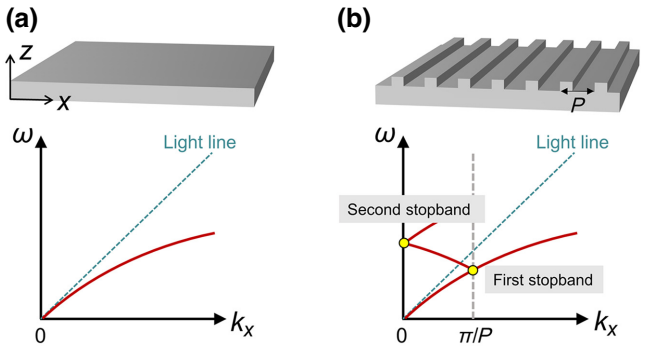

FIG. 2. Schematics of a regular slab waveguide (a) and a modulated waveguide (b) structure with both their dispersion diagrams.

dispersion diagram at $k_x = 2\pi/P$ or equivalently be folded to $k_x = 0$, which are referred to as the second stop band, and lays out the foundation for the well-known guided mode resonance (GMR) [24]. For the two frequencies, which constitute the spectral gap at the second stop band, one is usually related with an ideal BIC resonance, which cannot be excited while the other one usually has a Q factor generally small and significantly dependent on the magnitude of refractive-index modulation. The achievement of high-Q values with GMR is although possible but usually requires an extremely weak modulation of the refractive index and an extremely large device footprint [25]. Therefore, this conventional GMR is not preferred for excellent thermal-emitter performance.

However, when a period-doubling perturbation is induced into the periodic structure, e.g., by introducing ridge width difference δ in the interlaced ridges [shown in Fig. 3(a)], the period of the original lattice increases from P to $2P$. As a result, the FBZ shrinks from $(-\pi/P, \pi/P)$ to $(-\pi/2P, \pi/2P)$ in the wave-vector space and the band is folded at $k_x = \pi/2P$ [see Fig. 3(b)] instead of at $k_x = \pi/P$ as in the unperturbed lattice. Then the dispersion equation in the distorted lattice in $\omega - k$ space can be described by the equation:

$$f(-k_x) = f(k_x) = f(k_x - \pi/P). \quad (1)$$

The GMs with the spectral gap originally at $k_x = \pi/P$ will be flipped to be above the light line, which suggests the formation of an alternative set of leaky modes (QGMs) with the possibility of free-space excitations. We investigated the characteristics of the binary grating using the numerical approach of the finite-element method (FEM) implemented in the commercial software of COMSOL Multiphysics. Floquet periodic boundary conditions are applied in the x direction to define the wave vectors. Note that for simplicity we consider only the transverse electric (TE) mode with the electric field along the grating ridges in the y direction. Similar results can also be achieved for the transverse magnetic (TM) mode and due to the difference in the effective index of TE and TM modes, the emission wavelength for the TM mode will appear at a different wavelength.

The band structure for both the unperturbed grating and the binary grating with $\delta = 80$ nm are calculated and presented in Fig. 3(c). The red lines in the green shaded area below the light line are for the GMs supported in the original lattice, while the solid blue lines are the dispersion curves of the binary grating. It is clear that the latter are folded at the positions $k_x = \pm\pi/2P$ from the former, leading to the appearance of the modes originally at wave vectors close to π/P to be around $k_x = 0$ now, as indicated by the purple arrow. Here, the GM and QGM bands are labeled by GM_n and QGM_n, respectively, which represents the nth-order modes, and we consider only the GM_0 and QGM_0 modes in this work. Any resonance on the entire dispersion curve of the QGMs above the light cone has a high-Q factor (see Supplemental Material [22] for details), which can be flexibly adjusted by the level of perturbation. It is also seen at this value of $\delta = 80$ nm, which represents a weak perturbation, both the frequency and the profiles of the GM dispersion $f_0(x)$ (the red line) are almost identical to those of the QGMs in the distorted lattice. This is valid for any small perturbation, when we can assume that the profile of the dispersion diagram is not affected by the introduction of δ. In that case, Eq. (1) can be further described as

$$f(-k_x) = f(k_x) = f(k_x - 2\pi/2P) \approx f_0(k_x - \pi/P). \quad (2)$$

We further performed a two-dimensional mapping of the emissivity and absorptivity as a function of frequency and lateral wave vector within the FBZ for both the regular grating and the period-doubling perturbation-induced binary grating, and the results are presented in Figs. 3(d) and 3(e). It is clear from Fig. 3(d) that the GMRs supported by the regular grating have relatively broad emission bandwidths, which is consistent with our discussions of Fig. 2(b). However, for the distorted lattice, two alternative lines of emission resonances with ultranarrow linewidths emerge near the frequency $0.15c/P$, together with the presence of the same resonances as in Fig. 3(d) from GMRs between $0.25c/P$ and $0.3c/P$. This is consistent with the two QGM dispersion curves presented in Fig. 3(c), which visualizes the physical concept of the band-folding effect. The emissions from GMRs in the distorted lattice in Fig. 3(e) remain almost at the same position of the regular grating in Fig. 3(d), confirming the effect of a weak perturbation. In addition, the binary grating still exhibits a mirror symmetry with respect to the central plane of each ridge. For the two QGM dispersion curves at $k_x = 0$, two different modes with opposite symmetry are supported. When a linearly polarized plane wave impinges the binary grating normally, the mode with out-of-phase symmetry

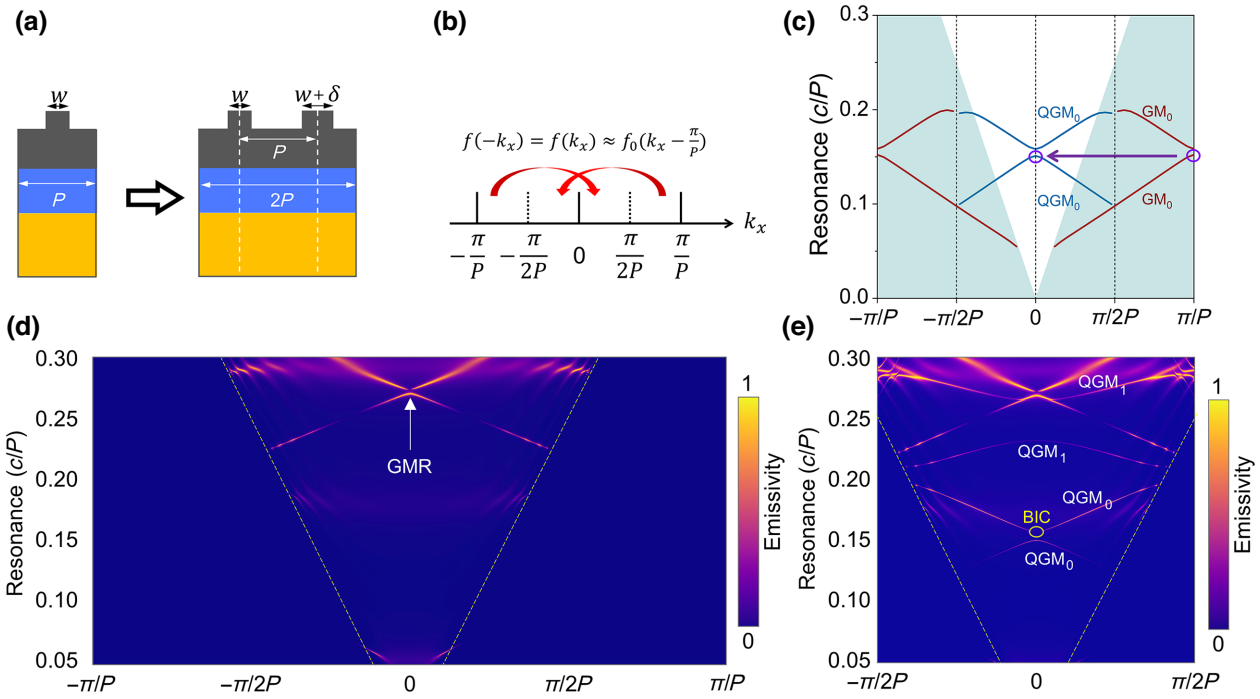

FIG. 3. (a) Schematic diagram of both the regular and the binary gratings after the introduction of the perturbation δ. (b) The idea of the FBZ folding and the frequency correspondence. (c) The calculated band structures of the regular grating (red solid lines) and the binary grating (blue solid lines) with $\delta = 80$ nm when the wave vector is along the k_x direction. 2D mapping of the emission spectrum within the FBZ using a regular grating (d) and the period-doubling perturbation induced binary grating (e).

within the waveguide layer cannot be excited because of a zero overlap integral between the incident wave and the mode distribution, forming a BIC of the symmetry-protected type at the Γ point. Therefore, when this structure of binary grating is used as a thermal emitter, there is only one output wavelength in the normal direction. Other than the normal direction, the structure has two emission peaks, whose wavelengths are dependent on the output angle over the entire frequency range of $0.05c/P$–$0.2c/P$. In addition, as the output angle increases, the two emission peaks have opposite shift trends, which can help realize the monochromaticity over a broad operation band with a fixed geometry.

We further studied the dependence of thermal-emission characteristics on the structural parameter. The temporal coherence of the thermal emissions is mostly affected by the total Q factor of a resonance [1]. As shown in Eq. (3), the total Q factor is determined by both the radiation Q factor (Q_{rad}) and absorption Q factor (Q_{abs}), which characterize the energy dissipation rates due to radiation and absorption losses, respectively.

$$Q = \left(\frac{1}{Q_{\mathrm{rad}}} + \frac{1}{Q_{\mathrm{abs}}}\right)^{-1}. \tag{3}$$

The achievement of a high-Q factor requires simultaneously high values of both Q_{rad} and Q_{abs}. However, in our fabrication of the structure, to simplify the experiments, all the material films were deposited by using the electron-beam evaporation (EBE). Therefore, the relationship between Q factor and δ was first calculated based on the eigenfrequency analysis for both cases with and without material loss [shown in Fig. 4(a)]. For the case of negligible material loss with epitaxially grown single-crystal materials, the Q factor reaches infinity as δ approaches 0, which corresponds to the case of unperturbed lattice with GMs. When the material losses are taken into account, the Q_{abs} will become finite but the Q factor can still reach the order of 10^3, which ensures the realization of ultranarrow bandwidth MIR thermal emitters (see Supplemental Material [22] for more discussions). Due to the practical limitations in experimental conditions, such as the fabrication defects and spectrometry resolution, a relatively large perturbation of $\delta = 80$ nm is chosen for both the simulation and experimental investigations of emission characteristics. The relationship between the resonance wavelength and Q factor with the x-direction wave vector was calculated and presented in Fig. 4(b). It is seen that the resonance is redshifted and the Q factor increases at a larger lateral wave vector, suggesting that the resonance belongs to the low-frequency branch of QGMs in Fig. 3(c). In other words, as the output angle increases, the emission spectrum redshifts, which provides a large range of frequency tuning to provide the spectral

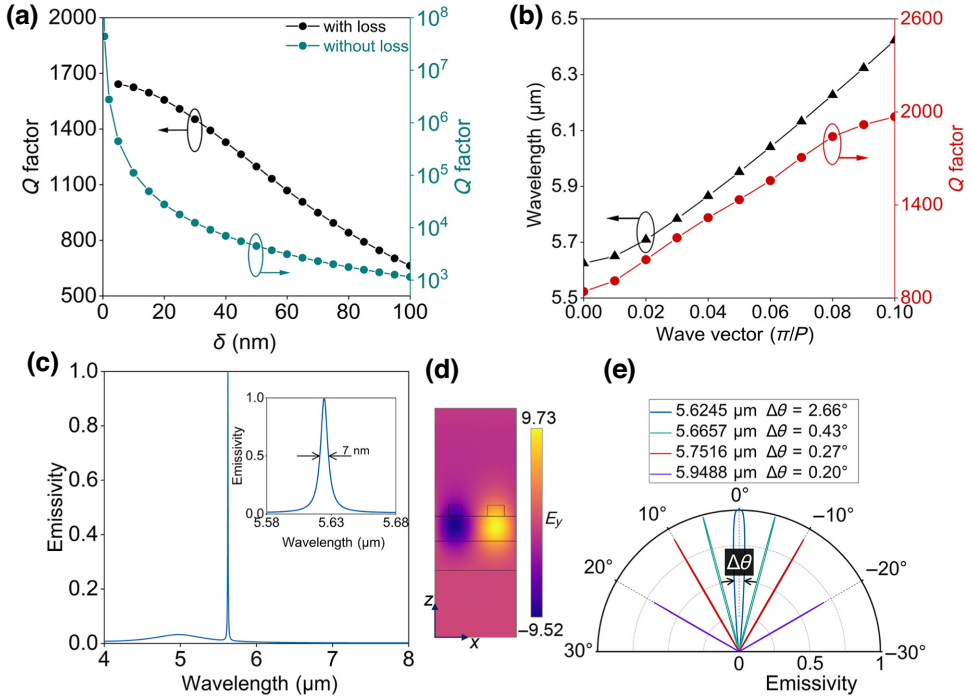

FIG. 4. (a) Dependence of the Q factor on the perturbation parameter δ. The black curve corresponds to the results with evaporated amorphous materials, while the green curve corresponds to the results where the losses of all materials are neglected. (b) Resonance wavelength and the associated Q factor of the QGMs as a function of k_x. (c) Normalized emission spectrum of the structure at normal direction and y polarization. The inset represents an enlarged view of the spectrum in the emission peak location. (d) The field distribution of the real part of E_y in the x-z plane at the emission peak. (e) The angular dependence of the emissivity on the output angle at different output wavelengths.

matching with the target absorption frequency in the MIR range. The calculated emission spectrum of the normal output in Fig. 4(c) show that there is only one major emission peak in the 4–8 μm wavelength range with near-unity emissivity, exhibiting good monochromatic performance. The inset gives a local magnification of the peak and demonstrates that a FWHM of about 7 nm can be achieved, which is approximately 2 orders of magnitude reduction in linewidth compared to conventional thermal emitters based on metallic metamaterials [26,27]. This large Q factor also means a similar level of enhancement in the temporal coherence can be achieved. Figure 4(d) shows the field distribution of the real part of E_y at the emission-peak wavelength, which is mainly concentrated in the high refractive-index waveguide layer directly below every ridge. The field also has an even-symmetric distribution across the central plane of each ridge, which ensures a nonzero coupling with the field of a plane wave. The out-of-phase distribution under adjacent ridges with the main field confined in the slab layer is consistent with that of the GM at the boundary of the FBZ. This mode can be efficiently excited by an incident plane wave, confirming the QGM characteristic of this resonance. Figure 4(e) also presents the calculated angular distribution of the thermal emission at three different output angles, each corresponding to a different central wavelength. The emissivity decreases sharply as the output angle increases, which suggests that a highly collimating and directional beam is emitted together with the monochromaticity. Particularly, at the wavelength around 5.95 μm, the FWHM of the emission angle is only about 0.2°. This small distribution angle corresponds to a spatial coherence length of $L_c = \lambda/\theta = 1.7$ mm, which is the highest value reported to date in the MIR.

We fabricated the designed structure on a silicon substrate (see Supplemental Material [22] for the fabrication details). Figure 5(a) shows the top and cross-section SEM images of the sample, which both exhibit a good accuracy with the design. The thermal radiation is characterized by using a FTIR spectroscopy with a commercial emission adapter to heat the whole sample to high temperatures. A home-made linear polarizer composed of Au lines on a CaF_2 substrate is introduced into the FTIR chamber to investigate the polarization property of the emission. All the collected emitting signals from the sample are normalized to those from a blackbody emitter, which is made from a steel plate smoked to be black and heated to the same temperature. The emission characteristics for the y polarization at 200 °C were first measured and shown as the solid blue line in Fig. 5(b). The inset shows its

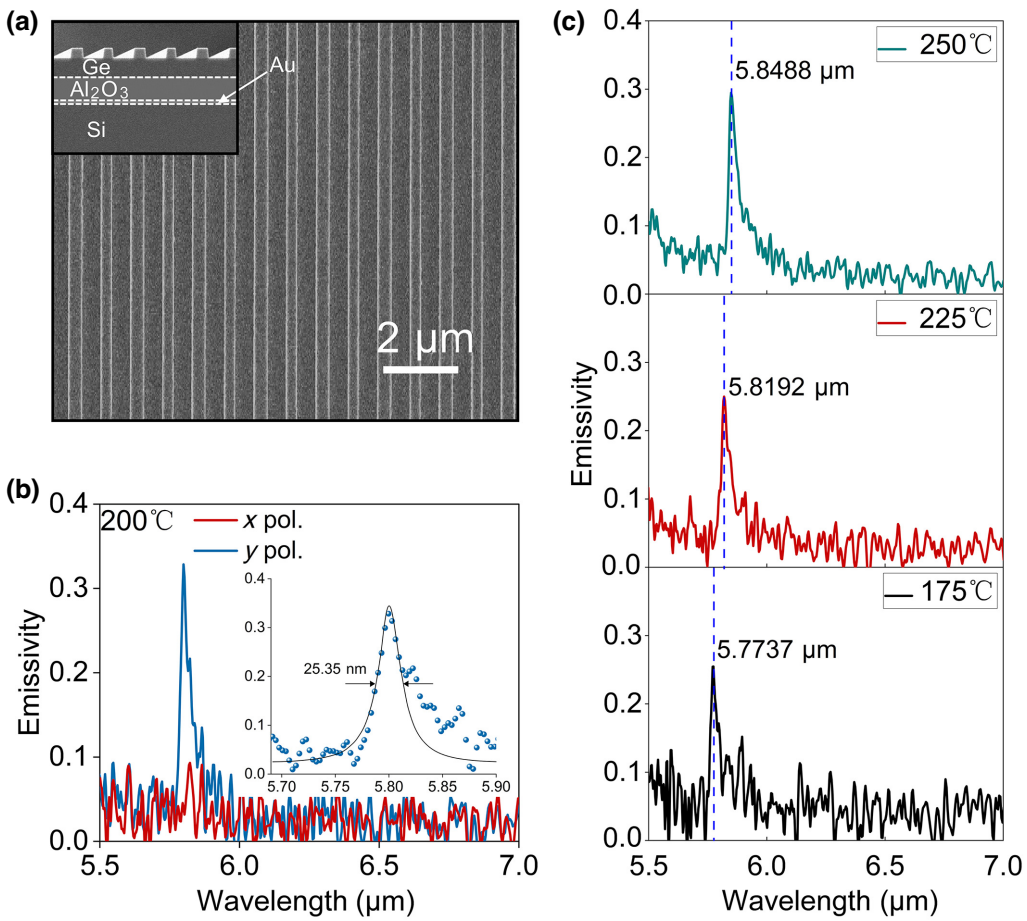

FIG. 5. (a) Top and cross-section views of the fabricated structure obtained with SEM. (b) Measured emission spectrum at 200 °C under x and y polarizations, respectively, normalized to a blackbody heated to the same temperature. (c) Normalized emission spectra at three other different temperatures (175, 225, and 250 °C). The blue dotted line represents the central position of the emission peak.

local magnification with a Lorentz linear fitting, which exhibits an emission wavelength of 5.7996 μm and bandwidth of 25.35 nm, corresponding to a Q factor of 229. The slightly lower Q value than the numerical results is mainly attributed to two reasons. First, the surface roughness of the fabricated device and the amorphous state of the films introduce additional optical losses. The mismatch between the Q_{abs} and Q_{rad} leads to a decrease of the emissivity from unity. According to the temporal coupled-mode theory [28], the absorptivity and emissivity reaches unity and maximum field enhancement is achieved when these two values are equal [19]. Second, the supported QGMs have a steep dispersion characteristic [see Fig. 4(b)] while the spectroscopy instrument captures the superposition of multiple thermal-emission peaks in a small angular range. This is similar to a scenario when a structure is excited by a focused light beam, leading to the excitation of multiple resonances at different wave vectors and a seemingly broadening of the resonance with a reduction in the overall Q factor [29,30] (see Supplemental Material [22] for more details). Thus the limitations of the instrument have a significant impact on our test results. The ultranarrow bandwidth emissions can also be tuned at different wavelengths within a wide spectral range, which has useful potential applications as tunable and monochromatic thermal radiation sources. Furthermore, the Q factors obtained experimentally in this work using our investigated structure are much higher than any other thermal emitters reported to date (see a comparison in the list in Table I), including traditional M-I-M structures ($Q < 40$), quantum well structures ($Q < 100$), and SPhP-based thermal emitters ($Q < 200$).

Finally, we verified the emission-polarization characteristics of the structure at 200 °C. As shown by the red solid line in Fig. 5(b), the emission peak disappears in this wavelength range when the structure works at the x polarization, indicating that the structure has good linear polarization characteristics. The emission spectra of the structures at three different temperatures, 175, 225, and 250 °C, were also measured and plotted in Fig. 5(c), all of which exhibit narrow emission linewidths. The signal-to-noise ratio is improved at higher temperatures. This is because the

TABLE I. Summary of recently reported experimental results for structured thermal emitters.

Year	Structures	λ (μm)	Q factor (exp.)	Refs.
2011	Au-*M*-*I*-*M* structure	5.8	∼8	[8]
2014	Quantum well structure	∼10	72	[31]
2015	Al-*M*-*I*-*M* structure	∼4.2	∼14	[32]
2015	Si_3N_4 on the TiN grating	3.06	43	[33]
2018	GST metasurface	∼3	5.4	[34]
2019	Au-*M*-*I*-*M* structure	5.83	∼32	[27]
2019	SiC metasurface	12.9	170	[35]
2020	Cu-*M*-*I*-*M* structure	4.227	18.5	[36]
2022	Ge grating on SIC	10.9	101	[37]
2023	Ge binary grating	∼5.8	>229	This work

main source of the noise signal is from the background blackbody radiations in the entirely heated thermal adapter, which is slightly blueshifted at higher temperatures and has less influence on the thermal-emitting signals in this spectral range. In practice, one can use a local electric heater, e.g., those based on the microelectromechanical system [26], then the background noise can be significantly eliminated. In addition, a slight redshift in the emission wavelength is observed at higher temperatures. As shown by the blue dashed line in Fig. 5(c), which marks the central emission wavelength, the emission shifts from 5.7737 μm at 175 °C to 5.8488 μm at 250 °C, while the Q factor remains almost unaffected. This is due to the fact that with the increase in temperature, the thermo-optic effect of Ge causes the real part of its refractive index to change slightly [38,39]. This shift can be utilized to offer an additional degree of freedom to adjust the resonance wavelength to precisely match the absorption of fine spectral structured matter.

III. DISCUSSIONS

We would like to emphasize that the main objective of the present work is to provide a proof-of-principle demonstration to show that a highly efficient thermal emitter based on the concept of QGMs can be achieved, thus providing and describing an extremely superior method of realizing high-performance thermal-radiation sources with both high temporal and spatial coherence. To simplify the experiments, all films were obtained by EBE, and the loss of the films obtained in this way was much higher compared to the corresponding single-crystal material. If single-crystal materials with more fancy techniques such as atomic layer deposition (ALD) or molecular beam epitaxy (MBE) are used to replace these amorphous materials obtained by EBE in practical applications, by flexibly tuning the δ value, the emission Q factor can be further improved to the orders of 10^4 or more.

The QGMs inherit the spatial dispersion of the original GMs, and thus have a strong dependence of the resonance frequency on the lateral wave vector. Although this characteristic suggests a tunability of the emission wavelength by choosing the emission angle, when the structure is heated to a high temperature, different output wavelengths are radiated towards different directions simultaneously. In our measurement setup, the radiations within an angular range enter the spectrometer (see Supplemental Material [22]). Because the spectrometer is equipped with multiple concave mirrors, the multiangle thermal radiations will be fully reflected into the detector, resulting in the collection of a superposition of multiple peaks, which increases the linewidth of the emission spectrum. In practical applications, this issue can be circumvented if the entire optical path of the collection system is optimized by incorporating spatial filters in front of the thermal emitters to select the radiations only towards certain emission angles.

We note that even with the existence of the above two detrimental effects in our work, an emission linewidth of 25 nm was still achieved experimentally. This is the narrowest linewidth thermal emitter ever achieved experimentally using a simple metasurface structure. If the above-mentioned strategy is to be used to further eliminate the influence from the material absorption and the setup deficiency, superior thermal emitters with the emission bandwidth close to that of the state-of-the-art quantum cascaded lasers can be expected.

Similar to the QBIC modes, the QGMs are also a collective response of infinite periodic structures. So in practical applications, one must design and manufacture a structure, which has a footprint large enough to accommodate the in-plane propagation of these spatially extending modes. Otherwise, the QBICs and QGMs will scatter at the edge of the structure into free space, which will deteriorate the high-Q properties. In contrast with QBIC modes, which inherit the vortexing property of BIC in the far-field polarizations [40], the QGMs are the derivatives of GMs and thus apt to have linear polarizations in the far field. In this means, we suggest that QGMs are more suitable for the generation of thermal emissions with linear polarizations while QBICs can be employed for circular polarizations instead. In addition, compared to QBIC, the QGMs are

more robust at different wave vectors because they are derivative of the GMs, which have extended dispersion curves. Thus thermal emissions from QGMs can have more flexibility in the tuning of frequency by the wave vector while the narrow bandwidth can be maintained at different output directions.

As a further remark, we should note that the thermal fluctuations in the metal substrate are random in both the orientation directions and amplitudes of the dipole momentums, which leads to the blackbody radiations described by Planck's law. In other words, the regular thermal emission is very like the spontaneous emission in nanophotonics, except that the excited energy level is very broad. When the binary grating supporting the QGMs are put in close proximity with the thermal fluctuations, the dipoles at the proper frequency will couple to the QGMs and then radiate with enhanced efficiency to free space. In this context, the whole process is very similar to the Purcell effect enhanced by optical nanoantennas [41], except that the required high local density of optical states are provided by the QGMs. In contrast with the plasmonic nanoantennas, the QGMs with high-Q factor and steep dispersion enable the enhanced thermal emissions with high temporal and spatial coherence. So the binary grating, although geometrically simple, works as a nonlocal metasurface [42] and provides the period-doubling perturbation, which is required to convert the infinite-Q GMs into QGMs with all the required properties.

IV. CONCLUSION

In summary, we have experimentally demonstrated that efficient thermal emitters with both high temporal and spatial coherence can be realized by making use of ultrahigh-Q factor QGMs generated by the band-folding effect in a binary grating structure. By perturbing the width of every second ridge in the periodic grating, the band-folding effect caused by the doubling of the period produces resonant modes with ultrahigh Q factors, which can be engineered to meet the demand for different resonance bandwidths. In addition to the high coherence, this thermal emitter has highly directionality, large spectral tunability and linear polarization properties and represent the state of the art in this direction. A greater number of ridges can be involved in the perturbation, e.g., to trigger a period-tripling perturbation [14] and this physics can be extended to the whole MIR or even THz by changing the geometric parameters. Such structures supporting the band-folding effect are not only suitable for 1D periodic grating but also suitable for 2D periodic structures. These results also suggest that the SPhP structures made from polar materials, employed in the literature to achieve the far-field narrowband thermal emissions, can be effectively replaced by the nonlocal metasurfaces. We believe that thermal emitters based on the band-folding effect stand for the next-generation MIR sources, and are useful for various applications in MIR optics.

ACKNOWLEDGMENT

This work is supported by the National Science Foundation of China (11974221, 12274269).

The authors have no conflicts to disclose.

[1] A. C. Overvig, S. A. Mann, and A. Alù, Thermal Metasurfaces: Complete Emission Control by Combining Local and Nonlocal Light-Matter Interactions, Phys. Rev. X **11**, 021050 (2021).

[2] N. Dahan, A. Niv, G. Biener, Y. Gorodetski, V. Kleiner, and E. Hasman, Enhanced coherency of thermal emission: Beyond the limitation imposed by delocalized surface waves, Phys. Rev. B **76**, 1 (2007).

[3] U. Willer, M. Saraji, A. Khorsandi, P. Geiser, and W. Schade, Near- and mid-infrared laser monitoring of industrial processes, environment and security applications, Opt. Lasers Eng. **44**, 699 (2006).

[4] Y. Gong, Z. Wang, K. Li, L. Uggalla, J. Huang, N. Copner, Y. Zhou, D. Qiao, and J. Zhu, Highly efficient and broadband mid-infrared metamaterial thermal emitter for optical gas sensing, Opt. Lett. **42**, 4537 (2017).

[5] L. Wang and B. Mizaikoff, Application of multivariate data-analysis techniques to biomedical diagnostics based on mid-infrared spectroscopy, Anal. Bioanal. Chem. **391**, 1641 (2008).

[6] Y. Yao, A. J. Hoffman, and C. F. Gmachl, Mid-infrared quantum cascade lasers, Nat. Photonics **6**, 432 (2012).

[7] T. Liu, C. Guo, W. Li, and S. Fan, Thermal photonics with broken symmetries, eLight **2**, 1 (2022).

[8] X. Liu, T. Tyler, T. Starr, A. F. Starr, N. M. Jokerst, and W. J. Padilla, Taming the Blackbody with Infrared Metamaterials as Selective Thermal Emitters, Phys. Rev. Lett. **107**, 045901 (2011).

[9] J. J. Greffet, R. Carminati, K. Joulain, J. P. Mulrt, S. Mainguy, and Y. Chen, Coherent emission of light by thermal sources, Nature **416**, 61 (2002).

[10] C. Guo, Y. Guo, B. Lou, and S. Fan, Wide wavelength-tunable narrow-band thermal radiation from moiré patterns, Appl. Phys. Lett. **118**, 131111 (2021).

[11] M. A. Kats, R. Blanchard, S. Zhang, P. Genevet, C. Ko, S. Ramanathan, and F. Capasso, Vanadium Dioxide as a Natural Disordered Metamaterial: Perfect Thermal Emission and Large Broadband Negative Differential Thermal Emittance, Phys. Rev. X **3**, 1 (2014).

[12] Z. Wang, J. K. Clark, Y. L. Ho, S. Volz, H. Daiguji, J. J. Delaunay, and J. J. Delaunay, Ultranarrow and wavelength-tunable thermal emission in a hybrid metal-optical Tamm state structure, ACS Photonics **7**, 1569 (2020).

[13] Z. Y. Yang, S. Ishii, T. Yokoyama, T. D. Dao, M. G. Sun, P. S. Pankin, I. V. Timofeev, T. Nagao, and K. P. Chen, Narrowband wavelength selective thermal emitters by confined Tamm plasmon polaritons, ACS Photonics **4**, 2212 (2017).

[14] K. Sun, H. Wei, W. Chen, Y. Chen, Y. Cai, and C. Qiu, Infinite-Q guided modes radiate in the continuum, Phys. Rev. B **107**, 115415 (2023).
[15] K. Sun, Z. Zhao, Y. Cai, U. Levy, and Z. Han, Ultra-narrowband and highly-directional THz thermal emitters based on the bound state in the continuum, Nanophotonics **10**, 4035 (2021).
[16] K. Koshelev, S. Lepeshov, M. Liu, A. Bogdanov, and Y. Kivshar, Asymmetric Metasurfaces with High-Q Resonances Governed by Bound States in the Continuum, Phys. Rev. Lett. **121**, 193903 (2018).
[17] F. Lemarchand, A. Sentenac, and H. Giovannini, Increasing the angular tolerance of resonant grating filters with doubly periodic structures, Opt. Lett. **23**, 1149 (1998).
[18] A.-L. Fehrembach, A. Talneau, O. Boyko, F. Lemarchand, and A. Sentenac, Experimental demonstration of a narrowband, angular tolerant, polarization independent, doubly periodic resonant grating filter, Opt. Lett. **32**, 2269 (2007).
[19] T. J. Seok, A. Jamshidi, M. Kim, S. Dhuey, A. Lakhani, H. Choo, P. J. Schuck, S. Cabrini, A. M. Schwartzberg, J. Bokor, E. Yablonovitch, and M. C. Wu, Radiation engineering of optical antennas for maximum field enhancement, Nano Lett. **11**, 2606 (2011).
[20] M. A. Ordal, R. J. Bell, R. W. Alexander, L. L. Long, and M. R. Querry, Optical properties of fourteen metals in the infrared and far infrared: Al, Co, Cu, Au, Fe, Pb, Mo, Ni, Pd, Pt, Ag, Ti, V, and W, Appl. Opt. **24**, 4493 (1985).
[21] R. Boidin, T. Halenkovič, V. Nazabal, L. Beneš, and P. Němec, Pulsed laser deposited alumina thin films, Ceram. Int. **42**, 1177 (2016).
[22] See Supplemental Material at http://link.aps.org/supplemental/10.1103/PhysRevApplied.20.024033 for details of the experimental investigations, including the fabrication processes and the optical measurement setup.
[23] R. Kazarinov and C. Henry, Second-order distributed feedback lasers with mode selection provided by first-order radiation losses, IEEE J. Quantum Electron. **21**, 144 (1985).
[24] G. Quaranta, G. Basset, O. J. F. Martin, and B. Gallinet, Recent advances in resonant waveguide gratings, Laser Photonics Rev. **12**, 1800017 (2018).
[25] A. C. Overvig, S. Shrestha, and N. Yu, Dimerized high contrast gratings, Nanophotonics **7**, 1157 (2018).
[26] A. Lochbaum, Y. Fedoryshyn, A. Dorodnyy, U. Koch, C. Hafner, and J. Leuthold, On-chip narrowband thermal emitter for mid-IR optical gas sensing, ACS Photonics **4**, 1371 (2017).
[27] S. Kang, Z. Qian, V. Rajaram, S. D. Calisgan, A. Alù, and M. Rinaldi, Ultra-narrowband metamaterial absorbers for high spectral resolution infrared spectroscopy, Adv. Opt. Mater. **7**, 1 (2019).
[28] H. A. Haus, *Waves And Fields In Optoelectronics* (Prentice-Hall, Englewood Cliffs, NJ, 1984).
[29] Y. Liang, H. Lin, S. Lin, J. Wu, W. Li, F. Meng, Y. Yang, X. Huang, B. Jia, and Y. Kivshar, Hybrid anisotropic plasmonic metasurfaces with multiple resonances of focused light beams, Nano Lett. **21**, 8917 (2021).
[30] L. Zundel, J. R. Deop-Ruano, R. Martinez-Herrero, and A. Manjavacas, Lattice resonances excited by finite-width light beams, ACS Omega **7**, 31431 (2022).
[31] T. Inoue, M. De Zoysa, T. Asano, and S. Noda, Realization of dynamic thermal emission control, Nat. Mater. **13**, 928 (2014).
[32] T. D. Dao, K. Chen, S. Ishii, A. Ohi, T. Nabatame, M. Kitajima, and T. Nagao, Infrared perfect absorbers fabricated by colloidal mask etching of Al-Al_2O_3-Al trilayers, ACS Photonics **2**, 964 (2015).
[33] J. Liu, U. Guler, A. Lagutchev, A. Kildishev, O. Malis, A. Boltasseva, and V. M. Shalaev, Quasi-coherent thermal emitter based on refractory plasmonic materials, Opt. Mater. Express **5**, 2721 (2015).
[34] T. Cao, X. Zhang, W. Dong, L. Lu, X. Zhou, X. Zhuang, J. Deng, X. Cheng, G. Li, and R. E. Simpson, Tuneable thermal emission using chalcogenide metasurface, Adv. Opt. Mater. **6**, 1800169 (2018).
[35] A. Howes, J. R. Nolen, J. D. Caldwell, and J. Valentine, Near-unity and narrowband thermal emissivity in balanced dielectric metasurfaces, Adv. Opt. Mater. **8**, 1901470 (2019).
[36] A. Lochbaum, A. Dorodnyy, U. Koch, S. M. Koepfli, S. Volk, Y. Fedoryshyn, V. Wood, and J. Leuthold, Compact mid-infrared gas sensing enabled by an all-metamaterial design, Nano Lett. **20**, 4169 (2020).
[37] B. Ma, Y. Huang, W. Zha, B. Qin, R. Qin, P. Ghosh, S. Kaur, M. Qiu, and Q. Li, Narrowband diffuse thermal emitter based on surface phonon polaritons, Nanophotonics **11**, 4115 (2022).
[38] H. H. Moore, Refractive index of alkaline earth halides and its wavelength and temperature derivatives, J. Phys. Chem. Ref. Data **9**, 161 (1980).
[39] K. H. Matsuo and T. Soma, Temperature dependence of the linear thermal expansion coefficient for Si and Ge, Phys. Status Solidi B **129**, K5 (1985).
[40] X. Zhang, Y. Liu, J. Han, Y. Kivshar, and Q. Song, Chiral emission from resonant metasurfaces, Science **377**, 1215 (2022).
[41] L. Novotny and N. Van Hulst, Antennas for light, Nat. Photonics **5**, 83 (2011).
[42] A. Overvig and A. Alù, Diffractive nonlocal metasurfaces, Laser Photonics Rev. **16**, 1 (2022).